Single-crystal investigations on the new multiferroic material LiFe$(\mathrm{WO}_4)_2$

S. Biesenkamp,[1] D. Gorkov,[1, 2] D. Brüning,[1] A. Bertin,[1] T. Fröhlich,[1] X. Fabreges,[3]
A. Goukassov,[3] M. Meven,[4, 5] P. Becker,[6] L. Bohatý,[6] T. Lorenz,[1] and M. Braden[1, *]
[1]*II. Physikalisches Institut, Universität zu Köln, Zülpicher Straße 77, D-50937 Köln, Germany*
[2]*FRM-II Munich, Germany*
[3]*Laboratoire Léon Brillouin, C.E.A./C.N.R.S., F-91191 Gif-sur-Yvette CEDEX, France*
[4]*RWTH Aachen University, Institut für Kristallographie, 52056 Aachen, Germany*
[5]*Jülich Centre for Neutron Science JCNS at Heinz Maier-Leibnitz Zentrum (MLZ)*
[6]*Abteilung Kristallographie, Institut für Geologie und Mineralogie,*
Universität zu Köln, Zülpicher Straße 49b, 50674 Köln, Germany
(Dated: November 13, 2020)

The crystal and magnetic structure of multiferroic LiFe$(\mathrm{WO}_4)_2$ were investigated by temperature and magnetic field dependent specific heat, susceptibility and neutron diffraction experiments on single crystals. Two different magnetic phases exhibiting long-range incommensurate order evolve at $T_{N1} \approx 22.2\,\mathrm{K}$ and $T_{N2} \approx 19\,\mathrm{K}$. First, a spin-density wave develops with moments along a direction in the ac plane and in its multiferroic phase below T_{N2}, LiFe$(\mathrm{WO}_4)_2$ exhibits a spiral arrangement with an additional b component. Therefore, the inverse Dzyaloshinskii-Moriya interaction fully explains the multiferroic behavior in this material. A partially unbalanced multiferroic domain distribution was observed even in the absence of an applied electric field. For both phases only a slight temperature dependence of the incommensurability was observed and there is no commensurate phase emerging at low temperature or at finite magnetic fields. LiFe$(\mathrm{WO}_4)_2$ thus exhibits a simple phase diagram with the typical sequence of transitions for a type-II multiferroic material.

I. INTRODUCTION

The demand of memory devices with larger storage capacity and less power consumption pushed the research on multiferroic materials featuring the coupling of magnetic ordering and ferroelectric polarization in the same phase (so called type-II multiferroics)[1–3]. During the past decades a variety of multiferroic systems were discovered and several different microscopic mechanism were identified to induce multiferroicity in respective materials [4, 5]. Beside symmetric exchange striction, the inverse Dzyaloshinskii-Moriya interaction (DMI) is a frequent mechanism that drives the multiferroic behavior in many type-II multiferroics [6–9]. With this mechanism, a spiral spin canting of neighboring spins induces a shift of nonmagnetic ligand ions and thus a ferroelectric polarization that can be controlled by external electric and magnetic fields. The spiral handedness (or precisely the vector chirality) determines the sign of the ferroelectric polarization.

Many multiferroic materials exhibit additional phase transitions at low temperature either due to other magnetic constitutents or due to locking into a commensurate phase. It was reported that anharmonic modulations of the spiral structure also cause sizable magnetoelastic coupling, which is different to the multiferroic one and which can lead to anomalous relaxation behavior of multiferroic domains[10, 11]. Beside the demand for higher transition temperatures and larger ferroelectric polarization it is also necessary to find multiferroic materials exhibiting simpler phase diagrams in order to analyze and describe multiferroic domain dynamics in these systems.

Recently, Liu et. al reported a type-II multiferroic phase in LiFe$(\mathrm{WO}_4)_2$ [12], which is beside MnWO_4 [13, 14] only the second multiferroic material in the family of tungstates and which exhibits much higher transition temperatures compared to related compounds [13–20]. In MnWO_4, the magnetic ions are occupying zigzag chains that are lying within the bc plane [21]. These chains are propagating along c direction and are separated along a by tungsten layers [21]. In case of the double tungstate NaFe$(\mathrm{WO}_4)_2$, an additional Na layer is intercalated between two tungsten layers thus doubling the distance between two magnetic zigzag chains and lowering the dimensionality of magnetic interaction [20]. Distinctive for LiFe$(\mathrm{WO}_4)_2$ is that the zigzag chains are not entirely occupied by magnetic ions but alternatingly by magnetic Fe^{3+} and by nonmagnetic Li^{1+} ions (see Fig. 1)[12, 20, 21]. Similar to MnWO_4 every second layer along a is magnetic in LiFe$(\mathrm{WO}_4)_2$.

Two successive magnetic anomalies have been reported at $T_{N1} \approx 22.6\,\mathrm{K}$ and $T_{N2} \approx 19.7\,\mathrm{K}$ and the first one was associated with the onset of short-range ordering [12]. At the lower transition an emerging ferroelectric polarization of about $15\,\mu\mathrm{C/m}^2$ was observed but the corresponding measurements were performed on polycrystalline samples thus preventing the determination of the polar axis [12]. Density-functional theory (DFT) calculations suggest a ferroelectric polarization along the b direction, whose magnitude is comparable to the one observed in MnWO_4 [12, 13, 22]. Neutron powder diffraction (NPD) revealed an incommensurate spiral ordering of magnetic moments below T_{N2} and thus suggests the inverse Dzyaloshinskii-Moriya interaction DMI as the un-

---

[*] e-mail: braden@ph2.uni-koeln.de

derlying mechanism for multiferroicity in $\mathrm{LiFe(WO_4)_2}$ [12]. No transition to a commensurate phase was observed and specific heat measurements reported only a slight magnetic-field dependence of both transitions indicating strong antiferromagnetic coupling as well as a simple phase diagram of $\mathrm{LiFe(WO_4)_2}$ [12].

However, NPD experiments are not sufficient to fully characterize complex magnetic structures in form of incommensurate spiral arrangements. Furthermore, it is unusual for spiral type-II multiferroics that short range magnetic ordering directly turns into a long-range spiral arrangement of magnetic moments without an intermediate phase [8, 23, 24]. A thorough investigation of the first magnetic transition at T_{N1} and confirmation of the spiral character below T_{N2} are thus needed requiring single-crystal investigations on $\mathrm{LiFe(WO_4)_2}$. Here we report on single-crystal investigations concerning the nuclear and magnetic structure utilizing different experimental techniques. After the introduction to experimental methods we will first discuss specific-heat data and the temperature dependent refinements of the nuclear structure before we subsequently discuss both observed magnetic phases, which have been characterized by susceptibility measurements, structural refinements and by neutron polarization analysis.

II. EXPERIMENTAL METHODS

Single crystals of about 3 mm × 3 mm × 0.5 mm in size were grown from a lithium poly-tungstate melt solution. The samples exhibit a finite conductivity even at low temperature, which prevented the application of electric fields and the direct investigation of the ferroelectric polarization. The measurements which are discussed below in the main section were performed on the same prepared single crystal SI. The investigations on a second sample SII exhibiting shifted transition temperatures are reported in the appendix A.

The characterization of the low-temperature phase transitions by susceptibility and by specific-heat measurements were done on a commercial superconducting quantum interference device (SQUID) magnetometer and on a commercial calorimeter (PPMS, Quantum Design) by using the thermal relaxation-time method. For the nuclear and magnetic structure determination, diffraction experiments with X-ray and neutron radiation have been executed. The respective single-crystal X-ray data collection for a refinement of the nuclear structure was carried out on a Bruker AXS Kappa APEX II four-circle X-ray diffractometer with MoK_α radiation ($\lambda = 0.7$ Å). An Oxford N-HeliX cryosystem was additionally deployed for low-temperature measurements. A collection of magnetic reflections as well as temperature and magnetic-field dependent Q space mappings of magnetic reflections were undertaken on the diffractometer 6T2, which is located at the Laboratoire Léon Brillouin (LLB). The instrument was equipped with a vertical cryomagnet ($\mu_0 H \leq 6$ T), a lifting counter detector and a vertically focusing pyrolytique graphite monochromator yielding a wavelength $\lambda = 2.35$ Å. A neutron diffraction experiment utilizing a polarized neutron beam was executed on the cold neutron three axes spectrometer KOMPASS, which is located at the FRMII. Serial polarizing V-shaped multichannel cavities provided an incoming polarized neutron beam and a highly oriented pyrolytic graphite (HOPG(002)) monochromator supplied $\lambda = 4$ Å. A split Helmholtz-Coil setup for defining the guide-field direction at the

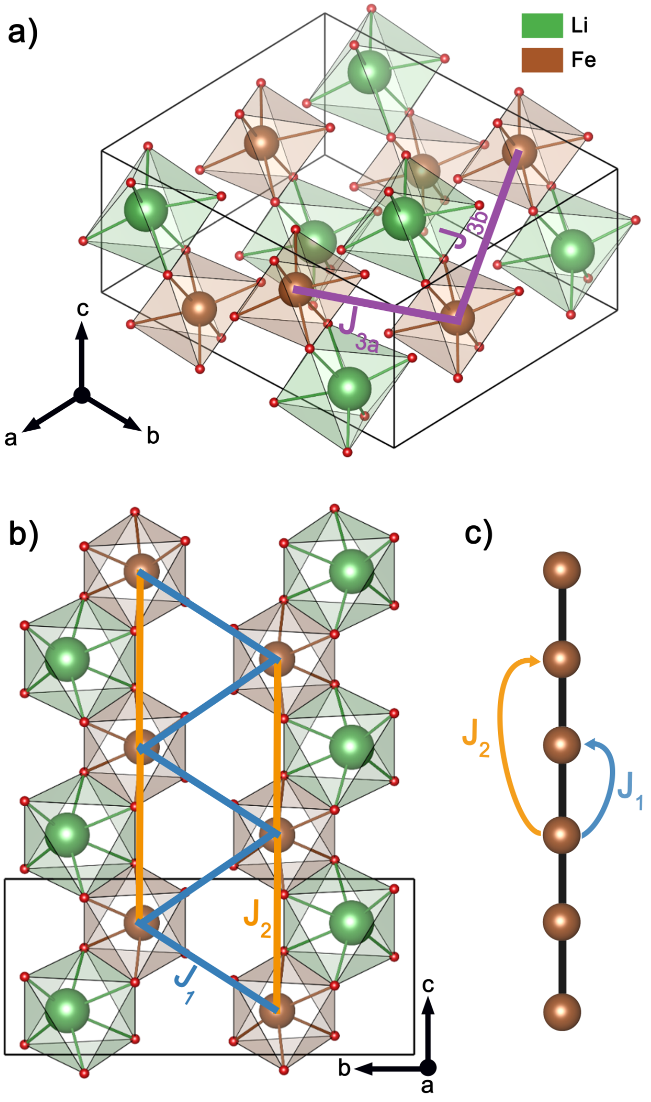

FIG. 1. Crystal structure and magnetic interaction paths in $\mathrm{LiFe(WO_4)_2}$. The views in a) and b) display the nuclear structure of $\mathrm{LiFe(WO_4)_2}$, for which the structural parameters were adopted from the refinement results based on X-ray diffraction data at 290 K (see table I). The respective exchange couplings J_i are marked by solid colored lines in both views and tungsten ions are hidden for the sake of simplicity. Figure c) visualizes the configuration of nearest-neighbor interaction J_1 and next-nearest neighbor interaction J_2 along the magnetic $\mathrm{Fe^{3+}}$ chain.

sample position was deployed together with a V-cavity polarizer in front of the detector thus enabling longitudinal polarization analysis.

III. RESULTS AND DISCUSSION

A. Nuclear structure

The nuclear structure was determined from X-ray and neutron diffraction data as a function of temperature. All atomic positions and isotropic displacement factors were refined by using the software JANA [25] and the corresponding results are summarized in table I.

Liu *et. al.* reported that $LiFe(WO_4)_2$ crystallizes in the monoclinic space group $C2/c$, which can be confirmed by our measurements. No superstructure reflections were observed as a function of temperature indicating no violation of the C centering or a structural transition. The system is composed of zigzag chains that are propagating along c direction (see Fig. 1). In contrast to $NaFe(WO_4)_2$ the nonmagnetic monovalent alkali-metal ion A in $AFe(WO_4)_2$ and the magnetic Fe^{3+} ions are not solely occupying the zigzag chains in $LiFe(WO_4)_2$ but alternating within the same chain. With respect to $MnWO_4$, the cell is not only doubled along a direction as it is the case in $NaFe(WO_4)_2$ but also along the b direction due to a phase shift of the Li^{1+} and Fe^{3+} ordering. In $NaFe(WO_4)_2$ the $[WO_6]$ octahedra layer separates nonmagnetic $[NaO_6]$ and magnetic $[FeO_6]$ layers, whereas in $LiFe(WO_4)_2$ the $[WO_6]$ units are intercalated between two layers that both contain magnetic Fe^{3+} ions.

By lowering the temperature to $T = 100\,K$ the respective inter- and intra-layer distances shrink by $\approx 0.3\,\%$, whereas a refinement at $T = 38\,K$ revealed no further significant length changes. We do not find any evidence for a structural phase transition and the low-temperature atomic displacement parameters are not enhanced.

TABLE I. This table contains the temperature dependent refinements of the nuclear structure based on single crystal X-ray data together with resulting reliabilty factors for structure factors. The temperature dependent lattice constants have been obtained by refining the orientation matrix considering the complete set of recorded X-ray data at the respective temperature. All refinements were done by using the software package JANA [25] and by assuming space group $C2/c$.

		x	y	z	U_{iso}
290 K	W	0.247505(9)	0.091348(9)	0.246221(18)	0.00299(3)
	Fe	0.0	0.33485(5)	0.25	0.00447(8)
	Li	0.5	0.3421(7)	0.25	0.008(2)
	O1	0.3634(2)	0.05909(18)	0.9240(4)	0.0052(3)
	O2	0.3801(2)	0.18198(19)	0.4114(4)	0.0056(3)
	O3	0.3552(2)	0.54862(18)	0.9452(4)	0.0052(3)
	O4	0.3769(2)	0.69430(19)	0.3928(4)	0.0059(3)
		Recorded reflections: 70005, Independent: 2816 a=9.2894(5), b=11.4142(6), c=4.9026(3), β=90.574(2), R(obs)=2.71, wR(obs)=3.08, R(all)=3.64, wR(all)=3.23			
100 K	W	0.24709(3)	0.09137(2)	0.24661(6)	0.00193(9)
	Fe	0.0	0.33466(13)	0.25	0.0019(2)
	Li	0.5	0.344(3)	0.25	0.031(11)
	O1	0.3635(6)	0.0586(5)	0.9252(11)	0.0032(8)
	O2	0.3800(7)	0.1830(5)	0.4121(12)	0.0063(10)
	O3	0.3557(6)	0.5485(5)	0.9446(11)	0.0047(9)
	O4	0.3781(6)	0.6946(5)	0.3936(11)	0.0037(9)
		Recorded reflections: 14973, Independent: 1595 a=9.252(4), b=11.383(4), c=4.8897(18), β=90.44(2), R(obs)=4.00, wR(obs)=3.67, R(all)=6.79, wR(all)=4.29			
38 K	W	0.24703(3)	0.09137(2)	0.24675(6)	0.00226(8)
	Fe	0.0	0.33474(13)	0.25	0.0025(2)
	Li	0.5	0.346(2)	0.25	0.022(5)
	O1	0.3638(6)	0.0598(5)	0.9245(10)	0.0050(8)
	O2	0.3801(6)	0.1822(5)	0.4115(10)	0.0051(8)
	O3	0.3562(5)	0.5497(5)	0.9437(10)	0.0045(8)
	O4	0.3775(5)	0.6951(5)	0.3933(10)	0.0046(8)
		Recorded reflections: 17924, Independent: 1681 a=9.2648(11), b=11.3858(13), c=4.8918(6), β=90.400(7), R(obs)=3.57, wR(obs)=3.45, R(all)=6.30, wR(all)=4.04			

B. Specific heat

Fig. 2 displays the temperature dependence of the specific heat for different magnetic fields applied along b and c. The C_p anomalies located at $T_{N1} \approx 22.2\,K$ and $T_{N2} \approx 19.0\,K$ agree with those from Liu *et. al.* [12]. As it can be seen in the inset b) of Fig. 2 no further anomalies were observed for higher temperatures up to room temperature. In magnetic fields up to 14 T along b, T_{N1} is essentially field-independent, while $T_{N2} = 19.0\,K$ reduces to 16.2 K. In contrast a magnetic field along c suppresses T_{N1}, while T_{N2} remains constant. This anisotropic behavior indicates different magnetic ordering phenomena at T_{N1} and T_{N2} and thus the presence of two different phases IC1 and IC2, which are studied in the following.

C. Susceptibility

The susceptibility was measured for magnetic fields applied along all crystallographic directions. As the crystal structure of $LiFe(WO_4)_2$ is monoclinic, the a direction is not equivalent to a^*, but because the monoclinic angle is close to 90°, the effect on the respective orientation is negligible. A detailed view of the low-temperature region is displayed in Fig. 3a). At $T_{N1} \approx 22.2\,K$ the susceptibility exhibits a significant sharp kink indicating the onset of long-range magnetic ordering. The susceptibility for fields applied along a and c direction starts to decrease below T_{N1}, whereas for a field applied along b direction, the susceptibility remains at the same level

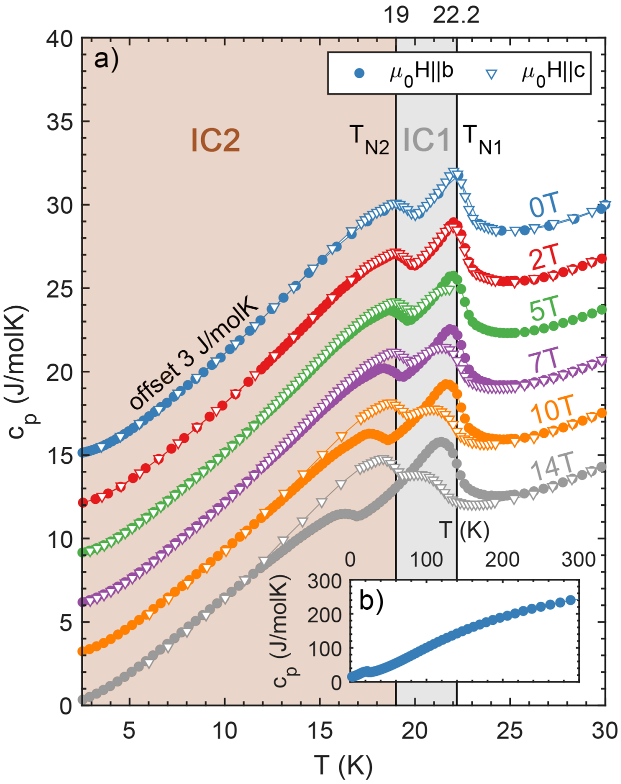

FIG. 2. In a), the specific heat of LiFe(WO$_4$)$_2$ in magnetic fields along b and c is shown. Different fields are offset by 3 J/molK. Both phases IC1 and IC2 are marked by colored regions and the respective transition temperatures T_{N1} and T_{N2} refer to the zero-field behavior. The zero-field data for temperatures up to room temperature are shown in the inset b).

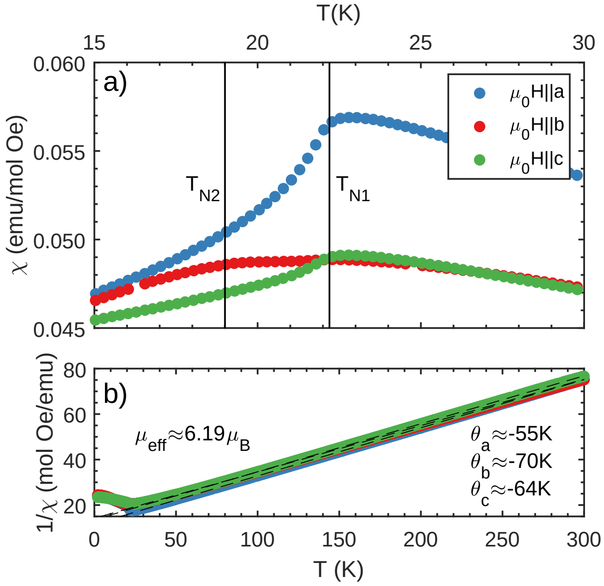

FIG. 3. Fig. a) displays the temperature dependence of the susceptibility χ for all crystallographic directions around the phase transitions T_{N1} and T_{N2}. The susceptibility was measured after zero-field cooling, while heating and applying a constant field of $\mu_0 H = 0.1\,\mathrm{T}$ to the sample. Curie-Weiss fits for $1/\chi$ are shown by dashed black lines in figure b) together with the resulting Weiss temperatures θ and the averaged effective moment μ_{eff}.

and decreases only below the second magnetic transition at $T_{N2} \approx 19\,\mathrm{K}$. Both transiton temperatures agree with the temperature of observed specific heat anomalies in Fig. 2, but T_{N1} and T_{N2} are slightly shifted against the transitions temperatures reported by Liu *et. al.* [12]. The temperature dependent susceptibility data suggests that magnetic moments are initially aligning within the ac plane and that an additional b component of the magnetic ordering is evolving below T_{N2}. This perfectly agrees with the impact of magnetic fields along b and c on T_{N1} and T_{N2} (see Fig. 2). The inverse susceptibility of the high temperature region was fitted by the Curie-Weiss function $C^{-1}(T+\theta)$ yielding antiferromagnetic Weiss temperatures for different field directions in the range of $\theta \approx -70\,\mathrm{K}$ to $-55\,\mathrm{K}$ (see Fig. 3b)). From this, the averaged effective magnetic moment $\mu_{\mathrm{eff}} \approx 6.19\mu_B$ was calculated and its value agrees well with the expected spin-only moment $\mu_{\mathrm{eff}} = 2\sqrt{S\,(S+1)} = 5.91\mu_B$ for Fe^{+3} $(S = 5/2, L = 0)$. The frustration parameter $f = |\theta|\,/T_N \approx 2.82$ is comparable to that in NaFe(WO$_4$)$_2$ ($f \approx 2$, see reference 20) and signals a moderate frustration with respect to the natural tungstate compound MnWO$_4$, which exhibits a larger frustration parameter of about 6 (see reference 13). In contrast to NaFe(WO$_4$)$_2$ no broad maximum was observed in LiFe(WO$_4$)$_2$ above the first magnetic transition thus indicating a more three-dimensional magnetic interaction. Compared to the low-dimensionality in NaFe(WO$_4$)$_2$ this is not astonishing, as the interlayer distance along a is significantly reduced, which enhances the magnetic interaction between layers and explains the higher antiferromagnetic transitions.

D. Incommensurate propagation vector

For tracing the temperature and magnetic-field dependence of evolving magnetic reflections and that of the incommensurability in LiFe(WO$_4$)$_2$ we performed experiments on the 6T2 diffractometer. A vertical cryomagnet ($\mu_0 H \leq 6\,\mathrm{T}$) was utilized together with a lifting counter detector that allows for the collection of reflections with a finite k component of the scattering vector $\boldsymbol{Q}$. For the respective experiment, the sample was mounted in the $(1\,0\,0)\,/\,(0\,0\,1)$ scattering plane thus aligning the b direction parallel to the magnetic-field.

Fig. 4 a) and b) display rocking scans over the magnetic reflections $\boldsymbol{Q} = (0.09\,{-1}\,{-1.3})$ and $\boldsymbol{Q} = (-2.09\,{-1}\,1.3)$ for $T = 3\,\mathrm{K}$ and $T = 20\,\mathrm{K}$, respectively. The indexation of both reflections yields similar h and l components of the incommensurate propagation vector $\boldsymbol{k}_{\mathrm{inc}} = (0.91\,0\,0.30)$ with respect to reference 12. For

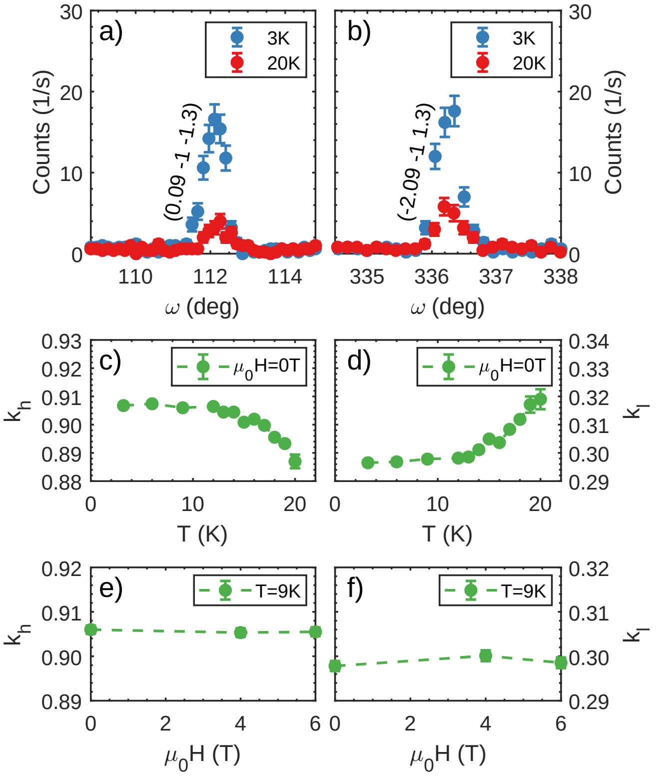

FIG. 4. Fig. a) and b) display rocking scans over the magnetic reflections $\boldsymbol{Q} = (0.09\ -1\ -1.30)$ and $\boldsymbol{Q} = (0.09\ -1\ -1.30)$ for $T = 3\,\text{K}$ and $T = 20\,\text{K}$ respectively. The temperature and magnetic field dependence of the incommensurate propagation vector $\boldsymbol{k}_{\text{inc}} = (k_h\ 0\ k_l)$ is shown in c) - f). All respective values have been obtained by fitting the Q-space mappings in the *h*-*l* plane with a two-dimensional Gaussian function. The magnetic field was applied along *b* direction.

TABLE II. Symmetry conditions for the transformation of the complex amplitudes u,v and w between both magnetic sites for the little group $G_{\boldsymbol{k}_{\text{ic}}} = \{1, c\}$. The conditions are purported by the irreducible representation Γ_1 and Γ_2 and the corresponding basisvectors Ψ with $a = e^{i2\pi 0.65}$. Equivalent results were reported in Ref. 12 .

Γ	Ψ	(x,y,z)	$(x,\bar{y},z+1/2)$
Γ_1	Ψ_1,Ψ_2,Ψ_3	(u,v,w)	$a(u,-v,w)$
Γ_2	Ψ_4,Ψ_5,Ψ_6	(u,v,w)	$a(-u,v,-w)$

both magnetic phases IC1 and IC2 a distinct peak is visible at the respective position in Q space. From this it can be stated that long-range magnetic order also persists in the IC1 phase. To trace the incommensurability in the respective magnetic phases, Q space mappings within the *h*-*l* plane were recorded around magnetic reflections as a function of temperature and magnetic field. Fig. 4 c) and d) show the temperature dependence of the resulting averaged h and l component of the incommensurate propagation vector for $\mu_0 H = 0\,\text{T}$ and it can be clearly seen that below T_{N1} the components of $\boldsymbol{k}_{\text{inc}}$ vary with temperature but reach a constant value at low temperature. Incommensurate magnetic long-range order persists down to low temperature contrarily to MnWO$_4$, which exhibits commensurate spin up-up-down-down (uudd) ordering at low temperatures [20, 21].

The magnetic field dependence of the incommensurability at $T = 9\,\text{K}$ is presented in Fig. 4 e) and f). In contrast to connatural NaFe(WO$_4$)$_2$, no variation of k_h and k_l is visible as a function of magnetic field strength. The absence of field dependent alteration of the incommensurability in LiFe(WO$_4$)$_2$ further illustrates a well-defined antiferromagnetic coupling in accordance with the simplicity of its phase diagram. Just two incommensurate magnetic phases exist at low temperature and persist for finite magnetic fields along b and c direction. The determination of the appropriate magnetic models and the refinement of the respective magnetic structure will be discussed in the following sections.

E. Magnetic structure of phase IC1 and IC2

In LiFe(WO$_4$)$_2$, the propagation vector remains incommensurate (see section III D). $\boldsymbol{k}_{\text{inc}}$ and -$\boldsymbol{k}_{\text{inc}}$ are not equivalent for both magnetic phases and thus two vectors belong to the star of $\boldsymbol{k}$. By considering space group $C2/c$ and the incommensurate propagation vector $\boldsymbol{k}_{\text{ic}} = (0.91\ 0\ 0.30)$, the little group $G_{\boldsymbol{k}_{\text{ic}}} = \{1, c\}$ can be deduced. The corresponding magnetic representation can be decomposed into two one-dimensional irreducible representations $\Gamma_{\text{mag}} = 3\Gamma_1 + 3\Gamma_2$. Both magnetic Fe sites on the 4f wyckoff position are linked via a c glide-plane symmetry and thus belong to one orbit. Therefore, only three complex amplitudes u,v,w are needed to describe the magnetic moment on each site. The phase difference between the two sites amounts $\phi_{\boldsymbol{k}} = 2\pi \times 0.65$ and the symmetry restrictions referring to the transformation of magnetic moments between the respective sites (x, y, z) and $(x,\bar{y},z + 1/2)$ are displayed in table II.

The collection of magnetic reflections in zero-field for both phases IC1 and IC2 was carried out on the 6T2 diffractometer by using the same setup as for the temperature and magnetic-field dependent study of the incommensurability (see section III D). Due to the instrumental setup the number of accessible reflections in Q space was limited, wherefore only 25 magnetic reflections have been recorded in the IC1 phase at $T = 20\,\text{K}$ and 39 magnetic reflections in the IC2 phase at $T = 3\,\text{K}$. The refinement and testing of different magnetic models was done with the software package FULLPROF[26]. All resulting reliability values for the refinements of respective models in both phases are displayed in table III and the observed versus calculated structure factors plots for the best resulting refinements are displayed in Fig. 5.

The best refinement result for the IC1 phase was unambiguously achieved by assuming a magnetic model that is compatible with the single irreducible representaion

TABLE III. The reliability values of refinements assuming different magnetic models at $T = 20\,\mathrm{K}$ and $T = 3\,\mathrm{K}$ respectively are displayed in this table. The refinement was done by using the FULLPROF suite[26].

	20 K		3 K		
	Γ_1	Γ_2	Γ_1	Γ_2	$\Gamma_1 \otimes \Gamma_2$
R_{F^2}	15.6	93.0	26.9	26.4	15.2
R_{wF^2}	18.5	87.4	25.2	28.9	15.3
R_F	19.6	74.0	20.4	17.3	13.4
χ^2	1.19	26.6	7.7	10.1	2.84

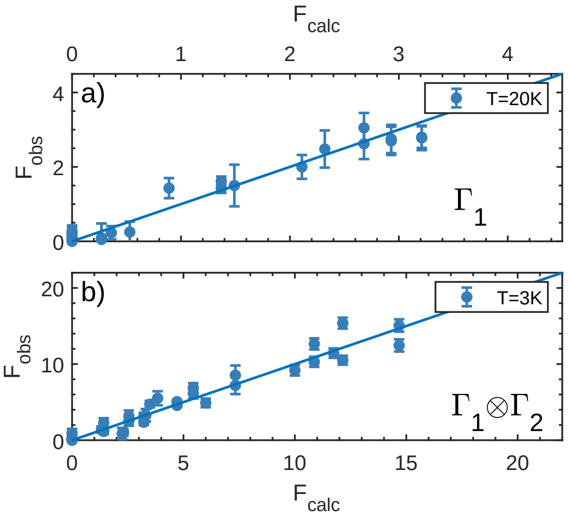

FIG. 5. Both plots a) and b) display the observed structure factors against the calculated ones for the magnetic models Γ_1 and $\Gamma_1 \otimes \Gamma_2$ at $T = 20\,\mathrm{K}$ and $T = 3\,\mathrm{K}$ respectively.

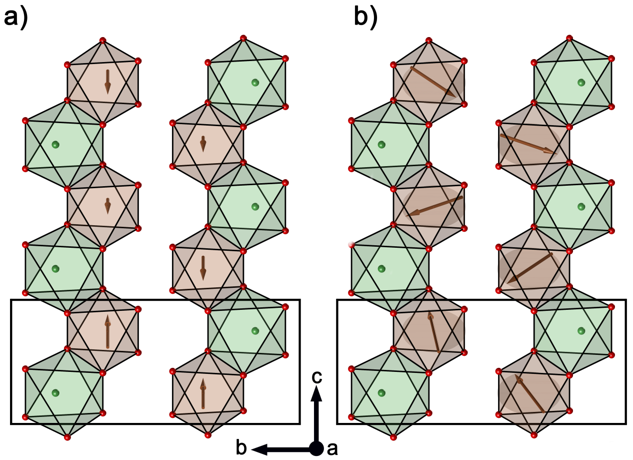

FIG. 6. The panels a) and b) visualize the refinement results for the magnetic structure in the magnetic phases IC1 and IC2 respectively. For the sake of simplicity intercalated tungsten ions are not shown.

Γ_1. Since for this phase, the susceptibility data indicates a magnetic arrangement exclusively lying within the ac plane and in order to reduce the number of parameters, the v component was fixed to zero. With this assumption, the magnetic moment on site 1 was refined to be $\boldsymbol{m} = (1.52(8)\ 0\ 1.33(10))\,\mu_B$ and thus the magnetic arrangement of the IC1 phase is described by a SDW that is confined to the ac plane with an easy axis $\boldsymbol{e}_{ac}$ that forms an angle of about 41° with the a axis. The alignment of moments almost bisecting the a and c directions nicely agrees the anomalies appearing in the susceptibility for magnetic fields along a and c.

Below T_{N2} an additional b component develops and the best refinement result was obtained by combining Γ_1 and Γ_2. The a and c components are described by Γ_1, whereas Γ_2 describes the b component. Moreover it turned out that choosing u, w to be real and v to be complex yield the lowest reliability values for the refinement and thus the magnetic model following $\Gamma_1 \otimes \Gamma_2$ describes an elliptical spin spiral arrangement for the IC2 phase with moments that are rotating within the plane spanned by $\boldsymbol{e}_{ac}$ and b. It has to be noted that the combination of two irreducible representations does not violate Landau theory, considering two consecutive second-order transitions, which is the typical scenario in many type-II multiferroics. The refinement yields $\boldsymbol{m} = (2.89(12)\ i2.52(14)\ 1.68(17))\,\mu_B$ and the length of the major and minor principal axes of the elliptical spiral amounts $m_{\max} = \sqrt{m_a^2 + m_c^2} \approx 3.34\ \mu_B$ and $m_{\min} = m_b \approx 2.52\ \mu_B$ respectively and hence depicting a moderate deformation with respect to a circular envelope. The averaged magnetic moment of the nearly circular spiral amounts $\approx 3.34\ \mu_B$, which is below the expected moment of Fe^{3+} due to magnetic frustration. $\mathrm{LiFe(WO_4)_2}$ does not exhibit a lower commensurate phase as $\mathrm{MnWO_4}$, thus making its phase diagram simple and comparable to the zero-field behavior of multiferroric $\mathrm{NaFeGe_2O_6}$ and $\mathrm{(NH_4)_2\,[FeCl_5\,(H_2O)]}$ [17, 27–30].

F. Neutron polarization analysis

Neutron polarization analysis can be used to separate the magnetic components and to sense the chirality of the magnetic structure. The respective experiment on $\mathrm{LiFe(WO_4)_2}$ was executed at the cold three axes spectrometer KOMPASS, located at the Forschungsreaktor-München (FRMII). The sample was mounted within the scattering plane $(1\,0\,0)\,/\,(0\,0\,1)$ and a Helmholtz coil setup was deployed for defining the guide field direction at the sample position. For a longitudinal polarization analysis the common right handed coordinate system was defined for which x is parallel to $\boldsymbol{Q}$, y perpendicular to x but within the scattering plane and z perpendicular to x and y. Thus, the crystallographic b direction is aligned parallel to z direction. The small sample volume demanded a high neutron flux for which reason the horizontal collimation in front of the secondary cavity was removed. As the efficiency of the V-shaped cavity

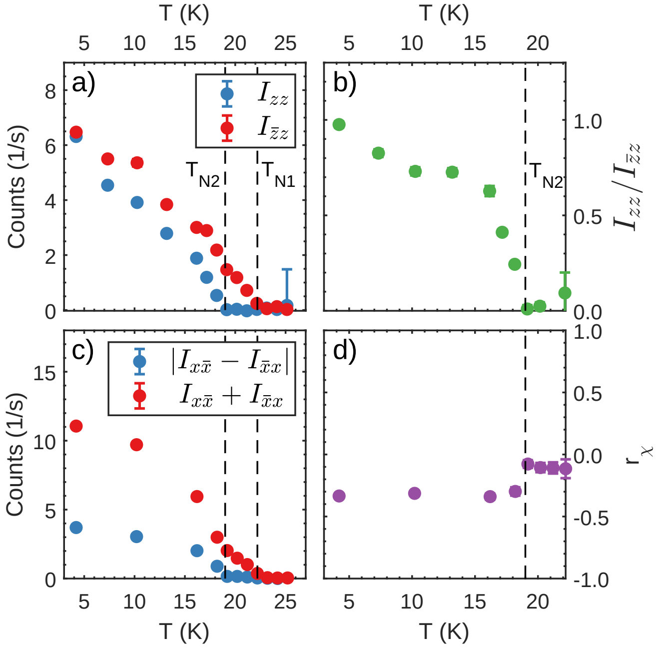

FIG. 7. The displayed intensities in a) correspond to the recorded NSF and SF channels I_{zz} and $I_{\bar{z}z}$ with $\boldsymbol{P}||z$ and $\boldsymbol{Q} = (0.91\,0\,0.30)$. Their ratio is plotted in b). In c) the sum and the difference of both SF channels with $\boldsymbol{P}||x$ are plotted and the respective quotient gives the chiral ratio r_χ, whose temperature dependence is plotted in d).

depends on the incoming beam divergence, the flipping ratio (FR) was reduced significantly to FR=8-11. However, the measured intensity for spin-flip (SF) and non spin-flip (NSF) channels can be corrected for a finite FR following Ref. 31. In the first part of the experiment, the neutron beam polarization was aligned parallel to z and a single spin-flipper was placed in front of the sample thus allowing to measure the SF channel $I_{\bar{z}z}$ and the NSF channel I_{zz}. The intensity for the respective SF and NSF channel was recorded for the magnetic reflection $\boldsymbol{Q} = (0.91\,0\,0.30)$ and their temperature dependence is displayed in Fig. 7a) respectively. Due to the chosen position in $\boldsymbol{Q}$ space, no nuclear Bragg signal contributes to the scattered intensity. In general, only the magnetization $\boldsymbol{M}_\perp(\boldsymbol{Q})$ perpendicular to $\boldsymbol{Q}$ contributes to the scattering process. Moreover, a neutron spin-flip requires a component of the magnetization perpendicular to the neutron beam polarization, whereas non-spin flip processes occur, when the beam polarization is parallel to the magnetization. Here, it entails that the respective SF and NSF channels are described by $I_{zz} = M_b M_b^*$ and $I_{\bar{z}z} = M_{ac} M_{ac}^*$ with M_b and M_{ac} being the complex fourier components of the magnetization along b direction and within the ac plane, respectively. From Fig. 7a) it can be clearly stated that in the IC1 phase a magnetic component is solely evolving within the ac plane. Below T_{N2} an additional b component develops and its magnitude approaches a similar size with respect to the ac component, when lowering the temperature. The respective temperature dependent ratio of both components is displayed in Fig. 7 b) and the qualitative statement is confirming the refinement results for both phases discussed above.

In the second part of the experiment, the neutron beam polarization was set parallel to x (parallel to $\boldsymbol{Q}$) and a second flipper was placed beyond the sample. With this configuration both SF channels $I_{x\bar{x}} = \boldsymbol{M}_\perp \boldsymbol{M}_\perp^* - i\,(\boldsymbol{M}_\perp \times \boldsymbol{M}_\perp^*)_x$ and $I_{\bar{x}x} = \boldsymbol{M}_\perp \boldsymbol{M}_\perp^* + i\,(\boldsymbol{M}_\perp \times \boldsymbol{M}_\perp^*)_x$ can be measured giving access to the chiral component $\pm i\,(\boldsymbol{M}_\perp \times \boldsymbol{M}_\perp^*)$, for which the sign depends on the handedness of the spiral. Fig. 7c) displays the sum and the difference of both SF channels hence presenting the temperature dependence of the overall magnetic scattering contribution $2\boldsymbol{M}_\perp \boldsymbol{M}_{\perp x}^*$ and that of the chiral signal $-i2\,(\boldsymbol{M}_\perp \times \boldsymbol{M}_\perp^*)$ respectively. It is cleary visible that a magnetic signal is arising below T_{N1}, whereas a chiral structure appears when passing the lower transition at T_{N2}. This is in accordance with the discussed refinement results, which proposed a SDW and a spiral spin arrangement below T_{N1} and T_{N2}, respectively. Fig. 7d) shows the calculated chiral ratio $r_\chi = (I_{x\bar{x}} - I_{\bar{x}x})\,/\,(I_{x\bar{x}} + I_{\bar{x}x})$ as a function of temperature. The chiral ratio gives the quotient of chiral scattering with respect to the total magnetic scattering contribution and has threshold values of ±1 for a respective monodomain state of a particular spiral handedness. Thus, the chiral ratio senses the multiferroic domain distribution but it has to be noted that the measured ratio for a monodomain state remains smaller because it depends on the $\boldsymbol{Q}$ vector orientation with respect to the spiral plane. Only for a scattering vector that is aligned perpendicular to the plane, chiral ratios of ±1 are observable. It can be seen in Fig. 7d) that a finite chiral ratio of about 0.3 appears below T_{N2} and thus exclusively within the multiferric phase. Astonishingly, the finite value of r_χ develops without an applied external electric field. The sample crystal thus exhibits an intrinsic preferred vector chirality.

G. Discussion of magnetic interaction and multiferroic coupling

The transition temperatures for both observed phases IC1 and IC2 are significantly larger than those reported for $\mathrm{NaFe(WO_4)_2}$ and $\mathrm{MnWO_4}$. The low transition temperatures in $\mathrm{NaFe(WO_4)_2}$ can be attributed to the reduced interlayer coupling arising from the separation through nonmagnetic Na layers. However, the lower transition temperatures in $\mathrm{MnWO_4}$ disagree with the higher density of magnetic $\mathrm{Mn^{2+}}$ compared to that of $\mathrm{Fe^{3+}}$ in $\mathrm{LiFe(WO_4)_2}$, which posses the same $3d^5$ configuration. The lower transition temperatures in $\mathrm{MnWO_4}$ result from a higher degree of frustration.

The magnetic coupling between $\mathrm{Fe^{3+}}$ ions in $\mathrm{LiFe(WO_4)_2}$ is mediated through super-super-exchange interaction along Fe-O-O-Fe and Fe-O-W-Fe paths, which are marked by J_1, J_2 and J_{3a}/J_{3b} in Fig. 1. The exchange coupling J_3 is split into J_{3a} and J_{3b} due to the moncolinic angle $\beta = 90.574(2)°$. The refinement based on single-crystal X-ray data at room temperature yields the inter- and intralayer distances between nearest-neighbor Fe ions of about 4.4970(10) Å, 4.9026(4) Å and 5.5773(5) Å/5.6180(5) Å for the pairs desribed by J_1, J_2 and J_{3a}/J_{3b}, respectively. In particular the distances of the pairs J_1 and J_2 are comparable so that a single zigzag chain is not the main magnetic unit. Instead the Fe^{3+} of two neighboring zigzag chains together form a magnetic chain with nearest-neighbor interaction J_1 and next-nearest neighbor interaction J_2, which is a classical configuration of frustration, see Fig. 1.

DFT calculations find J_1 to be ferromagnetic and J_2 and J_{3a}/J_{3b} to be antiferromagnetic yielding magnetic frustration [12]. The ferromagnetic coupling for J_1 can be verified by calculating the magnetic exchange energy in the incommensurate phase. For the SDW and the spiral phases the exchange energy per Fe resulting from J_1 and J_2 amounts to:

$$E_{\text{exch}} = -2J_1\cos(\pi q_c) - 2J_2\cos(2\pi q_c) \tag{1}$$

Only a ferromagnetic (positive) J_1 with $J_2/J_1 \approx -0.4$ agrees with the observed incommensurabilty along c of $\sim$0.3 in phases IC1 and IC2 (see section III D), which corresponds to a long wave length of about six Fe moments. However, $LiFe(WO_4)_2$ is not a highly one-dimensional system as the coupling between the double-zigzag chains are sizeable. Along the a direction there must be further frustration explaining the incommensurability along this direction.

In contrast to $NaFe(WO_4)_2$, no second intralayer spiral with opposite handedness exists as the upper and lower rows of a zigzag chain are alternatingly occupied by magnetic Fe^{3+} and nonmagnetic Li^{1+}. Furthermore spirals of neighboring layers possess the same handedness, wherefore the effect of inverse DMI is not canceled in $LiFe(WO_4)_2$. For the inverse DMI the ferroelectric polarization is given by

$$\boldsymbol{P} \propto \boldsymbol{r}_{ij} \times (\boldsymbol{S}_i \times \boldsymbol{S}_j) \tag{2}$$

with $\boldsymbol{S}_i$ and $\boldsymbol{S}_j$ being two neighboring spins and $\boldsymbol{r}_{ij}$ being the connecting vector of them [8, 9]. With this formalism we can determine the direction of the ferroelectric polarization. With the propagation vector (0.91 0 0.30) being perpendicular to b and with the spiral structure arising from e_{ac} and b components it is obvious that the four Fe moments coupled through J_1 and J_2 yield a ferroelectric polarization along the b direction. Taking into account all other pairs described by adding translations $\pm(n\boldsymbol{a}+m\boldsymbol{b}+l\boldsymbol{c})$ also shows that any polarization contribution perpendicular to b cancels out.

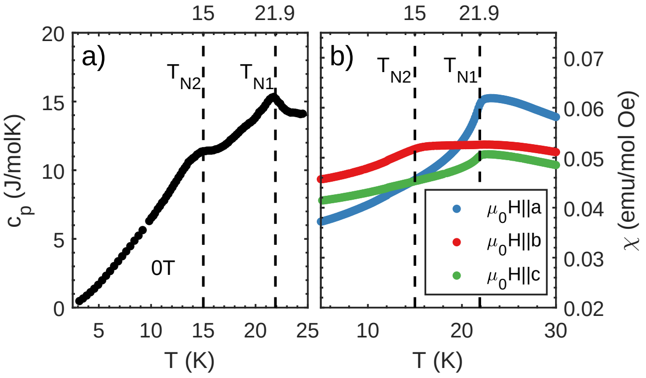

FIG. 8. The specific heat and susceptibility measurements were done on sample SII exhibiting shifted transition temperatures T_{N1} and T_{N2} with respect to sample SI. For the respective susceptibility measurments a magnetic field of $\mu_0 H = 0.1\,\mathrm{T}$ was applied.

IV. CONCLUSIONS

We presented a comprehensive investigation of the nuclear and magnetic structure of the newly discovered multiferroic material $LiFe(WO_4)_2$ [12]. The system undergoes two magnetic transitions at $T_{N1} \approx 22.2\,\mathrm{K}$ and $T_{N2} \approx 19\,\mathrm{K}$ to long-range incommensurate magnetic ordering. It was possible to determine the magnetic structure in both phases IC1 and IC2, revealing a SDW with an easy axis lying within the ac plane in phase IC1 and a spiral structure with an additional b component in phase IC2. The refined chiral structure of the IC2 phase is compatible with the proposed ferroelectric polarization along b direction following the inverse DMI [8, 9, 12] and it was observed that in IC2 an unbalanced multiferroic domain distribution appears even in the absence of an applied external electric field. The incommensurability in both magnetic phases shows only a slight temperature dependence, whereas the magnetic field does not change the magnetic propagation vector at all. No transitions to commensurate phases were observed, rendering the phase diagram simple and $LiFe(WO_4)_2$ a well suited material to study intrinsic multiferroic properties such as domain dynamics.

V. ACKNOWLEDGEMENTS

This work was funded by the Deutsche Forschungsgemeinschaft (DFG, German Research Foundation) - Project number 277146847 - CRC 1238, projects A02 and B04.

TABLE IV. This table shows nuclear refinements based on neutron diffraction data from sample SII for two temperatures. The refinement was done on structure factors and with the software Jana [25].

		x	y	z	U_{iso}
24 K	W	0.2477(2)	0.09126(14)	0.2470(4)	0.0028(4)
	Fe	0.0	0.33479(10)	0.25	0.0029(4)
	Li	0.5	0.3490(12)	0.25	0.014(4)
	O1	0.36282(14)	0.05850(11)	0.9253(3)	0.0045(4)
	O2	0.38005(13)	0.18264(12)	0.4103(3)	0.0049(4)
	O3	0.35572(14)	0.54899(12)	0.9430(3)	0.0044(4)
	O4	0.37748(13)	0.69389(11)	0.3928(3)	0.0042(4)
		Recorded reflections: 578, Independent: 290 R(obs)=2.12, wR(obs)=2.40, R(all)=2.35, wR(all)=2.42			
2.5 K	W	0.24762(16)	0.09120(12)	0.2470(3)	0.0029(3)
	Fe	0.0	0.33469(8)	0.25	0.0027(3)
	Li	0.5	0.3490(10)	0.25	0.018(4)
	O1	0.36296(11)	0.05854(9)	0.9254(3)	0.0044(3)
	O2	0.38022(11)	0.18271(10)	0.4104(3)	0.0049(3)
	O3	0.35587(11)	0.54909(9)	0.9428(3)	0.0040(3)
	O4	0.37741(11)	0.69373(9)	0.3925(3)	0.0047(3)
		Recorded reflections: 1259, Independent: 730 R(obs)=2.49, wR(obs)=2.52, R(all)=2.49, wR(all)=2.52			

Appendix A:

Characterization measurements on several $\mathrm{LiFe(WO_4)_2}$ samples revealed two different sample types that exhibit different transition temperatures. For some samples the specific heat as well as the susceptibility measurements display a slightly lowered value for T_{N1}, whereas the T_{N2} value was diminished significantly to $\approx$ 15 K. Exemplary measurements are shown for sample SII in Fig. 8. Sample SII was investigated furthermore by neutron diffraction at the four circle instrument HEIDI, which is located at the FRMII. A combined set of nuclear reflections was recorded with $\lambda = 0.795$ Å and $\lambda = 1.171$ Å utilizing a copper monochromator. The refinement of the nuclear structure yields similar results for the atomic positions (see table IV) compared to the structural refinement of sample SI (see table I). However, the structural refinement of sample SII discloses a mis-occupation of the Li-site by Fe ions of about 6.6(5) %, which provokes a strong impact on magnetic interactions and hence on the respective magnetic ordering and transition temperatures. In contrast, the X-ray experiment on sample SI yields a refined mis-occupation of only about 0.4(5) %. Thus, the discrepancy concerning the observed magnetic transition temperatures for both sample types and with respect to the reported phase diagram [12] of multiferroic $\mathrm{LiFe(WO_4)_2}$ arises from the alteration of the magnetic zigzag chains through a mis-occupation by Fe on the Li site. However, in both phases of SII, a magnetic reflection indexed by a similar propagation vector as for SI was detectable.

[1] J. F. Scott, "Multiferroic memories," Nat. Mater. **6**, 256 (2007).

[2] M. Fiebig, "Revival of the magnetoelectric effect," J. Phys. D. Appl. Phys. **38**, R123 (2005).

[3] N. A. Spaldin and R. Ramesh, "Advances in magnetoelectric multiferroics," Nat. Mater. **18**, 203 (2019).

[4] M. Fiebig, T. Lottermoser, D. Meier, and M. Trassin, "The evolution of multiferroics," Nature Reviews Materials **1**, 16046 (2016).

[5] D. Khomskii, "Classifying multiferroics: Mechanisms and effects," Physics **2**, 20 (2009).

[6] I. E. Dzyaloshinskii, "A thermodynamic theory of "weak" ferromagnetism of antiferromagnetics," J. Phys. Chem. Solids **4**, 241 (1958).

[7] T. Moriya, "Anisotropic Superexchange Interaction and Weak Ferromagnetism," Phys. Rev. **120**, 91 (1960).

[8] M. Mostovoy, "Ferroelectricity in Spiral Magnets," Phys. Rev. Lett. **96**, 067601 (2006).

[9] T. Kimura, "Spiral Magnets as Magnetoelectrics," Annu. Rev. Mater. Res. **37**, 387 (2007).

[10] M. Baum, J. Leist, T. Finger, K. Schmalzl, A. Hiess, L. P. Regnault, P. Becker, L. Bohatý, G. Eckold, and M. Braden, "Kinetics of the multiferroic switching in MnWO$_4$," Phys. Rev. B **89**, 1 (2014).

[11] S. Biesenkamp, N. Qureshi, Y. Sidis, P. Becker, L. Bohatý, and M. Braden, "Structural dimerization in the commensurate magnetic phases of NaFe(WO$_4$)$_2$ and MnWO$_4$," Phys. Rev. B **102**, 144429 (2020).

[12] M. Liu, L. Lin, Y. Zhang, S. Li, Q. Huang, V. O. Garlea, T. Zou, Y. Xie, Y. Wang, C. Lu, L. Yang, Z. Yan, X. Wang, S. Dong, and J.-M. Liu, "Cycloidal magnetism driven ferroelectricity in double tungstate LiFe(WO$_4$)$_2$," Phys. Rev. B **95**, 195134 (2017).

[13] K. Taniguchi, N. Abe, T. Takenobu, Y. Iwasa, and T. Arima, "Ferroelectric polarization flop in a frustrated magnet MnWO$_4$ induced by a magnetic field," Phys. Rev. Lett. **97**, 097203 (2006).

[14] O. Heyer, N. Hollmann, I. Klassen, S. Jodlauk, L. Bohatý, P. Becker, J. A. Mydosh, T. Lorenz, and D. Khomskii, "A new multiferroic material: MnWO$_4$," J. Phys. Condens. Matter **18**, L471 (2006).

[15] T. Kimura, T. Goto, H. Shintani, K. Ishizaka, T. Arima, and Y. Tokura, "Magnetic control of ferroelectric polarization," Nature **426**, 55 (2003).

[16] G. Lawes, A. B. Harris, T. Kimura, N. Rogado, R. J. Cava, A. Aharony, O. Entin-Wohlman, T. Yildirim, M. Kenzelmann, C. Broholm, and A. P. Ramirez, "Magnetically driven ferroelectric order in Ni$_3$V$_2$O$_8$," Phys. Rev. Lett. **95**, 087205 (2005).

[17] M. Ackermann, D. Brüning, T. Lorenz, P. Becker, and L. Bohatý, "Thermodynamic properties of the new multiferroic material (NH$_4$)$_2$[FeCl$_5$(H$_2$O)]," New Journal of Physics **15**, 123001 (2013).

[18] M. Ackermann, L. Andersen, T. Lorenz, L. Bohatý, and P. Becker, "Anisotropy study of multiferroicity in the pyroxene NaFeGe$_2$O$_6$," New Journal of Physics **17**, 013045 (2015).

[19] S. Jodlauk, P. Becker, J. A. Mydosh, D. I. Khomskii, T. Lorenz, S. V. Streltsov, D. C. Hezel, and L. Bohatý, "Pyroxenes: a new class of multiferroics," Journal of Physics: Condensed Matter **19**, 432201 (2007).

[20] S. Holbein, M. Ackermann, L. Chapon, P. Steffens, A. Gukasov, A. Sazonov, O. Breunig, Y. Sanders, P. Becker, L. Bohatý, T. Lorenz, and M. Braden, "Strong magnetoelastic coupling at the transition from harmonic to anharmonic order in NaFe(WO$_4$)$_2$ with $3d^5$ configuration," Phys. Rev. B **94**, 104423 (2016).

[21] G. Lautenschläger, H. Weitzel, T. Vogt, R. Hock, A. Böhm, M. Bonnet, and H. Fuess, "Magnetic phase transitions of MnWO$_4$ studied by the use of neutron diffraction," Phys. Rev. B **48**, 6087 (1993).

[22] A. H. Arkenbout, T. T. M. Palstra, T. Siegrist, and T. Kimura, "Ferroelectricity in the cycloidal spiral magnetic phase of MnWO$_4$," Phys. Rev. B **74**, 184431 (2006).

[23] P. Tolédano, "Pseudo-proper ferroelectricity and magnetoelectric effects in tbmno$_3$," Phys. Rev. B **79**, 094416 (2009).

[24] P. Tolédano, B. Mettout, W. Schranz, and G. Krexner, "Directional magnetoelectric effects in MnWO4: magnetic sources of the electric polarization," Journal of Physics: Condensed Matter **22**, 065901 (2010).

[25] V. Petříček, M. Dušek, and L. Palatinus, "Crystallographic computing system JANA2006: General features," Zeitschrift für Krist. **229**, 345 (2014).

[26] J. Rodríguez-Carvajal, "Recent advances in magnetic structure determination by neutron powder diffraction," Physica B: Condensed Matter **192**, 55 (1993).

[27] I. Kim, B.-G. Jeon, D. Patil, S. Patil, G. Nénert, and K. H. Kim, "Observation of multiferroic properties in pyroxene NaFeGe$_2$O$_6$," Journal of Physics: Condensed Matter **24**, 306001 (2012).

[28] L. Ding, P. Manuel, D. D. Khalyavin, F. Orlandi, and A. A. Tsirlin, "Unraveling the complex magnetic structure of multiferroic pyroxene NaFeGe$_2$O$_6$: A combined experimental and theoretical study," Phys. Rev. B **98**, 094416 (2018).

[29] J. Alberto Rodríguez-Velamazán, Ó. Fabelo, Á. Millán, J. Campo, R. D. Johnson, and L. Chapon, "Magnetically-induced ferroelectricity in the (ND$_4$)$_2$[FeCl$_5$(H$_2$O)] molecular compound," Sci. Rep. **5**, 14475 (2015).

[30] W. Tian, H. Cao, J. Wang, F. Ye, M. Matsuda, J.-Q. Yan, Y. Liu, V. O. Garlea, H. K. Agrawal, B. C. Chakoumakos, B. C. Sales, R. S. Fishman, and J. A. Fernandez-Baca, "Spin-lattice coupling mediated multiferroicity in (ND$_4$)$_2$[FeCl$_5$(H$_2$O)]," Phys. Rev. B **94**, 214405 (2016).

[31] T. Chatterji, Neutron Scattering from Magnetic Materials (Elsevier Science, 2005).